International Journal of Power Electronics and Drive System (IJPEDS)
Vol. 17, No. 4, December 2026, pp. 2865~2878
ISSN: 2088-8694, DOI: 10.11591/ijpeds.v17.i4.pp2865-2878

Performance enhancement of three-level inverter PV systems using modified ADRC and fractional-order PID control

Gherici Dinar[1], Ahmed Tahour[2]
[1]LSTE Laboratory, University Mustapha Stambouli of Mascara, Mascara, Algeria
[2]École Supérieure en Sciences Appliquées de Tlemcen, Tlemcen, Algeria

Article Info

Article history:

Received Oct 7, 2025
Revised Aug 2, 2026
Accepted Aug 14, 2026

Keywords:

FOPI-MPPT
Grid
Grid tide PV system three-level inverter
MADR controller
THD

ABSTRACT

The increasing global adoption of solar energy requires control schemes that ensure reliable operation and high power quality under varying environmental conditions. In grid-connected applications, three-level inverters reduce current distortion and improve power quality compared with conventional two-level topologies. This study presents a two-stage control framework for a three-level grid-connected photovoltaic (PV) inverter. On the power-harvesting side, a fractional-order proportional-integral (FOPI) controller performs maximum power point tracking (MPPT), ensuring rapid convergence under changing solar irradiance. On the grid side, a modified active disturbance rejection controller (MADRC) is proposed as an alternative to conventional ADRC. The proposed MADRC incorporates an inner regulation loop based on Lyapunov stability to maintain the DC-link voltage and enhance disturbance rejection. MATLAB/Simulink simulations compare the proposed FOPI–MADRC scheme with a conventional incremental conductance (INC)–ADRC configuration. The INC–ADRC system achieves 233.45 kW with a grid-current total harmonic distortion (THD) of 2.87%, whereas the proposed scheme increases the extracted power to 246.32 kW and reduces THD to 0.43%. These results demonstrate that combining a three-level inverter with FOPI-based MPPT and MADRC grid-side control improves PV power extraction, DC-link regulation, and grid-current quality under changing operating conditions.

This is an open access article under the CC BY-SA license.

Corresponding Author:

Gherici Dinar
LSTE Laboratory, University Mustapha Stambouli of Mascara
Mascara, Algeria
Email: dnr.ghrc@gmail.com

1. INTRODUCTION

The intensifying demand for energy, attributable to demographic pressures and the parallel expansion of industry and agriculture, underscores the pressing need for alternative clean energy resources [1]. The transition to sustainable energy systems continues to be challenged by fossil fuels, which are both depleting and environmentally harmful [2]. In this context, renewable energy sources (RES) have emerged as fundamental components of future energy infrastructures, prized for their natural abundance and reduced environmental impacts [3], [4]. In particular, photovoltaic (PV) systems present a promising pathway; however, their operational variability in response to climatic conditions necessitates the adoption of advanced control strategies and refined MPPT methods to ensure consistent and efficient interconnection with the utility grid [5].

Among the various renewable alternatives, solar PV technology stands out for its scalable design, favorable operating costs, and suitability for both standalone and grid-connected installations [6]. However, the reliability of these systems remains constrained by the intermittent nature of sunlight, the physical limits

on conversion efficiency, and the strongly nonlinear voltage-current characteristics of PV generators [7], [8]. Left unaddressed, these factors can lead to unstable direct current (DC)-link voltage, reduced energy yield under fast-changing weather, and degraded grid current quality due to increased harmonic distortion at the inverter stage [9]. At the cell level, conversion efficiency remains fundamentally bounded by material-dependent factors such as the semiconductor absorption coefficient and photoanode layer quality [10], [11].

Multilevel converter topologies offer a compelling means of resolving these difficulties [12]. Compared with conventional two-level structures, three-level neutral point clamped (NPC) inverters achieve better harmonic reduction and improved alternating current (AC) voltage quality, making them well suited for PV-grid integration, although switching losses increase with the higher number of semiconductor devices [12], [13]. Still, achieving optimal system performance depends heavily on advanced control strategies able to handle nonlinear dynamics, external disturbances, and parameter uncertainties. The efficiency and power quality requirements of modern grid-connected PV systems often exceed the capabilities of classical controllers (PI, LADRC) and conventional maximum power point tracking (MPPT) algorithms (P&O, INC), despite their widespread usage.

Existing contributions to grid-connected PV regulation have largely treated MPPT enhancement and grid-side control as distinct research tracks. Regarding power extraction, LMI-based regulators [14] have demonstrated improvements in tracking fidelity and harmonic suppression, yet often neglect the overall PV conversion efficiency as a performance metric. Concerning grid interaction, voltage-oriented control implemented on a three-level diode-clamped grid-side converter (GSC) [15] succeeded in reducing current total harmonic distortion (THD) while overlooking system-level efficiency. Previous research has also investigated ADRC and MADRC strategies for multilevel NPC inverters in grid-connected PV systems [16]. At the same time, comparative evaluations of multilevel topologies employing nonlinear control frameworks such as integral backstepping alongside ADRC/LADRC modifications incorporating deviation-based compensation have repeatedly highlighted the three-level NPC arrangement as delivering the optimal equilibrium between stability and resilience. Despite these contributions, however, one aspect that remains insufficiently addressed is the development of a holistic framework that simultaneously enhances MPPT precision and grid-side disturbance attenuation within a unified multilevel architecture.

Motivated by the preceding discussion, this study presents a two-stage control architecture for a three-level NPC PV inverter, employing a FOPI regulator for MPPT and a MADRC framework for grid-side control. In contrast to conventional strategies based on INC and similar MPPT methods, the proposed FOPI–MADRC scheme is specifically evaluated for its capacity to simultaneously improve power extraction and reduce grid-current THD within the three-level topology. The paper is organized as follows: i) Section 2 covers system modeling; ii) Section 3 describes controller design; iii) Section 4 presents simulation results and discussion; and iv) Section 5 concludes the paper.

2. METHOD

2.1. Structure of the studied system and mathematical model

The system under study, depicted in Figure 1, comprises a 250 kW PV array, a DC-DC boost converter dedicated to MPPT, and a voltage source inverter (VSI) equipped with an RL filter. This inverter, serving as the grid-side converter (GSC), is responsible for delivering the generated AC power to the utility grid.

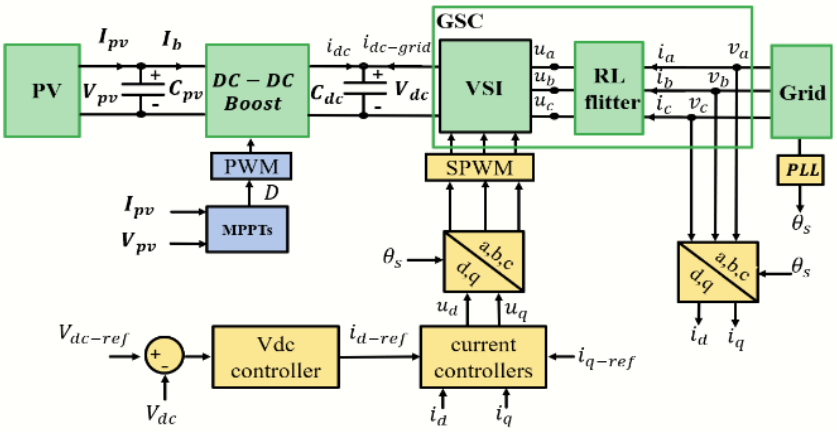

Figure 1. The structure of the studied system

2.2. Modeling of the photovoltaic cell

As shown in Figure 2, the PV array is modeled using the widely adopted single-diode equivalent circuit, which comprises a current source, a diode, and both series and parallel resistances [17]-[19]. The resulting current-voltage characteristic is expressed by (1).

$$I_{PH} - I_D - \frac{V_D}{Rsh} - I_{pv} = 0 \quad (1)$$

The PV array output current, I_{pv}, can be expressed as (2)-(4). The diode reverse saturation current is given by (2).

$$\text{Irs} = \text{Iscref} + [e^{\left(\frac{qVoc}{NsKAT}\right)} - 1] \quad (2)$$

The saturation current of the module, I_0, is obtained from (3).

$$\text{Io} = \text{Irs}[\frac{(\frac{T}{Tref})^3}{AK} e^{qCg} * \left(\frac{1}{Tref} - \frac{1}{T}\right)] \quad (3)$$

Finally, Figure 2 presents the equivalent model used to describe the photovoltaic current, which can be mathematically formulated as (4).

$$\text{Ipv} = \text{IscNp} - \text{NsIo}\left[e^{\frac{qVpv+IpvRs}{NsAKT}} - 1\right]\text{Vpv} + \frac{IpvRs}{Rsh} \quad (4)$$

The parameters employed in the above equation are defined hereunder. The principal electrical variables consist of Ipv, the PV module output current; Id, the diode current; and Isc, the short-circuit current. The diode-specific parameters include Irs (reverse saturation current) and I_0 (saturation current). The diode voltage is denoted by Vd, and Rsh represents the shunt resistance, which models leakage current losses. Additionally, K is the Boltzmann constant, and T denotes the absolute temperature expressed in Kelvin.

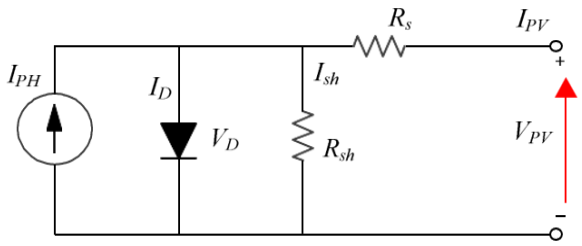

Figure 2. Equivalent model of single diode solar cell

2.3. Boost converter model

The DC–DC boost converter performs two essential functions. First, it steps up the photovoltaic array output voltage to a value suitable for the inverter and grid interconnection. Second, it regulates the DC-link voltage at a constant level, which is imperative for ensuring reliable inverter performance and mitigating voltage oscillations that could compromise power quality. Additionally, the converter furnishes the suitable framework for deploying MPPT algorithms, facilitating optimal energy capture from the PV array across diverse environmental conditions. Consequently, it serves a central role in reinforcing system robustness and flexibility when transferring power toward the grid or supplying local loads. The dynamic behavior of this boost stage is described in (5) and (6) [20], and the corresponding circuit configuration with load is depicted in Figure 3.

$$\frac{dI_L}{dt} = \frac{-(1-D)}{L}V_{out} + \frac{1}{L}V_{in} \quad (5)$$

$$\frac{dV_{out}}{dt} = \frac{(1-D)}{C_{out}}I_L - \frac{1}{RC_{out}}V_{out} \quad (6)$$

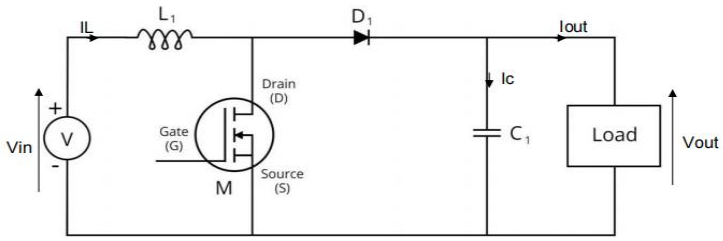

Figure 3. DC-DC boost converter model

2.4. Modeling of the DC-bus voltage dynamics

The DC link serves as a critical interface between the boost converter and the VSI, providing temporary energy buffering and ensuring regulated power transfer between the two stages. By maintaining equilibrium between the PV-side and grid-side power flows, this stage effectively attenuates disturbances that could otherwise impair the quality of the converted AC power. Furthermore, it sustains a stable DC-bus voltage, which is essential for precise grid current regulation and for controlling active and reactive power exchange. The DC-link voltage is governed by the following relationship:

$$\frac{dV_{dc}}{dt} = \frac{1}{C_{dc}}(i_{dc} + i_{dc-grid}) \quad (7)$$

2.5. Three-level neutral point clamped inverter

Several multilevel converter configurations exist, including the NPC topology, the cascaded H-bridge arrangement, and the flying capacitor structure. For this work, the NPC topology depicted in Figure 4 was selected owing to its advantageous characteristics for solar power conversion. In comparison with alternative configurations, it demands fewer power semiconductors and capacitive elements, thereby reducing overall complexity, hardware expenses, and switching-related energy losses [21]. Moreover, the NPC inverter is capable of synthesizing multiple voltage levels with diminished harmonic content, thereby yielding enhanced voltage quality at the output [12]. This feature makes it particularly attractive for renewable-based integration, where power quality constitutes a primary concern. Furthermore, the inherent symmetry in DC-link capacitor utilization within the NPC configuration promotes more stable operation and extends the service life of individual components [13]. Nevertheless, realizing these benefits hinges upon a well-designed control architecture, as the regulation strategy directly influences both the efficiency of power transfer to the grid and the overall dependability of the PV installation. Taken together, these attributes establish the NPC topology as a compelling candidate for elevating the performance of contemporary grid-tied renewable energy systems.

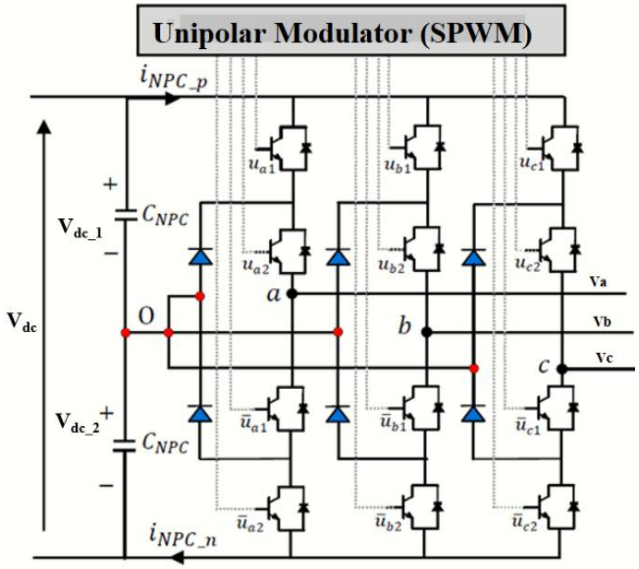

Figure 4. the topology of the three levels NPC inverter used in this paper

2.6. The grid-side converter model

In renewable-energy-based generation systems—encompassing wind, wave, solar, and other technologies—the GSC enables bidirectional power exchange with the utility grid by performing the primary conversion between the DC-link voltage, Vdc, and the AC voltage. The dynamics of the GSC are commonly expressed in the synchronous dq-reference frame as (8) and (9) [22]-[24].

$$\frac{di_d}{dt} = \frac{1}{L_{filter}}(-R_{filter}i_d + \omega_s L_{filter}i_q + V_d - u_d) \quad (8)$$

$$\frac{di_q}{dt} = \frac{1}{L_{filter}}(-R_{filter}i_q - \omega_s L_{filter}i_q + V_q - u_q) \quad (9)$$

Where id, iq are the d- and q-axis currents; Vd, Vq are the grid voltages; ud, uq are the inverter output voltages; L_{filter} and R_{filter} are the filter parameters; and ωs is the grid angular frequency.

3. CONTROL SYSTEMS DESIGN

3.1. Voltage-oriented regulation of the GSC

The control strategy for the GSC is characterized by two primary objectives. The outer loop regulates the DC-link voltage to its setpoint, Vdc−ref, whereas the inner loop manages the active and reactive power injections, with the latter assigned a zero reference. Under the assumption of synchronous frame alignment with the grid voltage vector, Vs, such that the d-axis corresponds to Vs and Vq=0, the resulting power equations are expressed as (10) and (11) [22]-[24].

$$P = 1.5V_d i_d = V_{dc}i_{dc-grid} \quad (10)$$

$$Q = -1.5V_d i_q \quad (11)$$

Unity power factor is achieved by setting the q-axis current reference, iq, to zero. Consequently, the GSC control scheme is organized along two main axes: The q-axis is responsible for holding i_q at its null reference. As for the d-axis, it relies on a cascaded regulation structure comprising two loops: the outer loop maintains the DC-link voltage in accordance with its target value, while the inner loop regulates the current *id* based on the reference supplied by this outer voltage regulator.

3.1.1. FOPID control of DC-link voltage

The fractional-order PID (FOPID) controller is a sophisticated control technique that permits fractional-order integration and differentiation, hence expanding the capabilities of the traditional PID. This adaptability makes it possible to fine-tune the dynamics of the system more precisely, enhancing stability, transient responsiveness, and disturbance resistance. It is especially useful in nonlinear and complex systems where conventional PID controllers could find it difficult to sustain peak performance. Overshoot, settling time, and steady-state error can all be better balanced by modifying the fractional orders in addition to the gains [25]-[27]. The FOPID controller can be mathematically expressed in its general form as (12) [28].

$$C(s)_{FOPID} = \frac{U(s)}{E(s)} = k_P + \frac{k_i}{S^{\lambda}} + k_d S^{\mu} \ (\lambda, \mu \geq 0) \quad (12)$$

In this formulation, C(s) designates the FOPID controller's transfer function, while E(s) and U(s) correspond to the input error and output signals, respectively. Figure 5 illustrates the arrangement of this control strategy for regulating the DC-link voltage. The control law, u(t), can be written in the time domain as (13).

$$U(t) = k_P + K_i D^{-\lambda} e(t) + k_d D^{\mu} e(t) \quad (13)$$

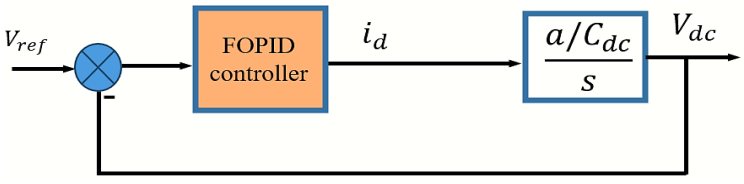

Figure 5. The block diagram for controlling the DC link voltage using FOPID controller

3.1.2. ADR control of DC-link voltage

As discussed above, active disturbance rejection control (ADRC), originally developed by Han, has emerged as an effective control strategy for systems subject to uncertainties and disturbances [29], [30]. Recent studies have also demonstrated the applicability of ADRC to renewable-energy systems, including photovoltaic-based systems, for mitigating disturbances and improving control robustness [31]. The linearized version (LADRC) combines a proportional gain (k_p), with an extended state observer (ESO) that estimates both the system states and the total disturbance, which aggregates internal and external perturbations. Nonlinear error feedback (NLSEF) then generates the control signals necessary for accurate and stable reference tracking [30]. By lumping all uncertainties into a single term, this approach compensates for unmodeled dynamics using only the measured output [32], [33]. For the present study, under the simplifying condition iq=0, the DC-link voltage (7) is reformulated as (14).

$$\frac{dV_{dc}}{dt} = \frac{1}{C_{dc}} i_{dc} + \frac{a}{C_{dc}} i_d \tag{14}$$

Where the coefficient *a* is tied to the GSC transformation ratio. This expression can be equivalently written in the compact form (15).

$$\frac{dV_{dc}}{dt} = f(.) + b_0 u \tag{15}$$

Where:

$$f(.) = \frac{1}{C_{dc}} i_{dc},\ u = i_{d-ref}, b_0 = \frac{a}{C_{dc}} \tag{16}$$

The ADR regulator for the DC bus is subsequently constructed through the following observer-controller formulation, where the ESO tracks both the state and the total disturbance in (17)-(21).

$$\frac{d\widehat{V_{dc}}}{dt} = \hat{f}(.) + b_o u - B_1 e_1 \tag{17}$$

$$\frac{d\hat{f}(.)}{dt} = -B_2 e_1 \tag{18}$$

$$e_1 = \widehat{V_{dc}} - V_{dc} \tag{19}$$

$$i_{d-ref} = \frac{u_o - \hat{f}(.)}{b_o} \tag{20}$$

$$u_o = k_p\ (V_{dc-ref}\ - \widehat{V_{dc}}) \tag{21}$$

The ADRC-based DC-link voltage control architecture is illustrated in Figure 6.

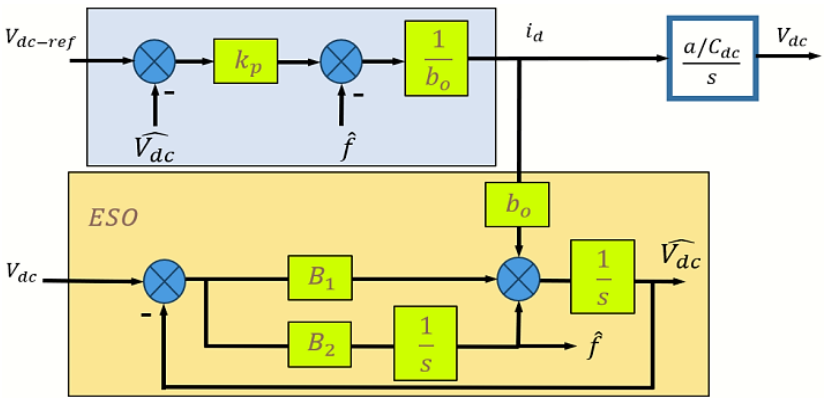

Figure 6. The ADRC-based DC-link voltage regulation block diagram

3.1.3. MADR control of DC-link voltage

By neglecting the external disturbance term in (7), the expression reduces to (22).

$$\frac{dV_{dc}}{dt} = \frac{a}{C_{dc}} i_d \tag{22}$$

Suppose the following error relationship in (23).

$$e_3 = V_{ref} - k_n V_{dc} \tag{23}$$

Differentiating (22) and substituting the corresponding terms yields (24).

$$\dot{e_3} = -k_n \frac{a}{C_{dc}} i_d \tag{24}$$

Assuming a Lyapunov function (25).

$$V = 0.5 e_3^2 \tag{25}$$

Substituting (25) into the time derivative of the Lyapunov function yields (26).

$$\dot{V} = -e_3 k_n \frac{a}{C_{dc}} i_d \tag{26}$$

The reference current i_d is determined by the following control law (27).

$$i_d = k \frac{C_{dc}}{k_n a} e_3 \tag{27}$$

Substituting (27) into the relationship (26), we find (28).

$$\dot{V} = -k e_3^2 \tag{28}$$

Thus, a strictly positive value for the gain *k* must be selected to guarantee system stability. By substituting (27) and (23) into (22), one obtains the following differential equation, which expresses the transfer function linking V_{ref} to V_{dc}:

$$\frac{dV_{dc}}{dt} = -kV_{dc} + \frac{k}{k_n} V_{ref} \tag{29}$$

The expression in (29) may be recast as follows:

$$\frac{dV_{dc}}{dt} = f(.) + b_0 u \tag{30}$$

Where:

$$f(.) = -kV_{dc},\ u = V_{ref}, b_0 = \frac{k}{k_n} \tag{31}$$

Using (30), the redesigned ADR scheme for DC-link regulation is expressed as (32).

$$\frac{d\widehat{V_{dc}}}{dt} = \hat{f}(.) + b_o V_{ref} - B_1 e_2 \tag{32}$$

$$\frac{d\hat{f}(.)}{dt} = -B_2 e_2 \tag{33}$$

$$e_2 = \widehat{V_{dc}} - V_{dc} \tag{34}$$

$$V_{ref} = \frac{u_o - \hat{f}(.)}{b_o} \tag{35}$$

$$u_o = k_p\ (V_{dc-ref}\ - \widehat{V_{dc}}) \tag{36}$$

Figure 7 presents the block diagram for DC-link voltage regulation using MADRC.

3.2. MPPT control system

The nonlinear P-V characteristics of the studied PV system are depicted in Figure 8. Under standard test conditions (1000 W/m², 25 °C), the simulation results show that the output power attains a peak value of approximately 248.8 kW. Furthermore, an increase in irradiance results in a higher MPP value, whereas a temperature rise produces the opposite effect, lowering the MPP. To ensure maximum power extraction at any specific irradiance and temperature, the operating voltage must be kept strictly at its optimum point. Any variation away from this optimum, whether upward or downward, directly diminishes the harvested power and prevents the system from operating at its peak. Consequently, it is essential to implement a robust MPPT algorithm that can continuously adjust the operating point, thereby maintaining optimal system performance across varying atmospheric conditions.

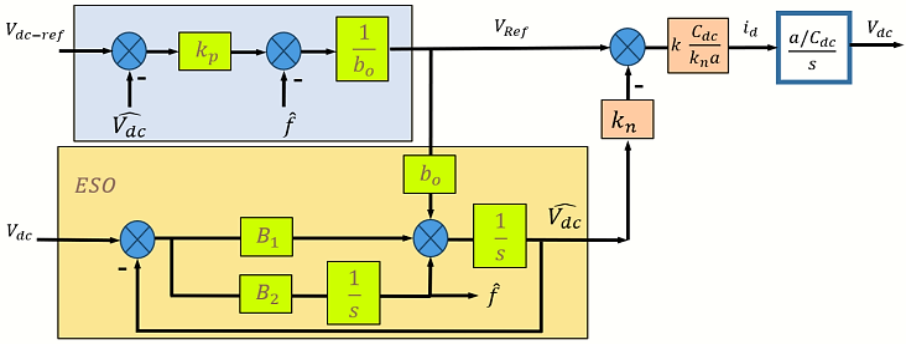

Figure 7. The block diagram for controlling the DC link voltage using MADRC

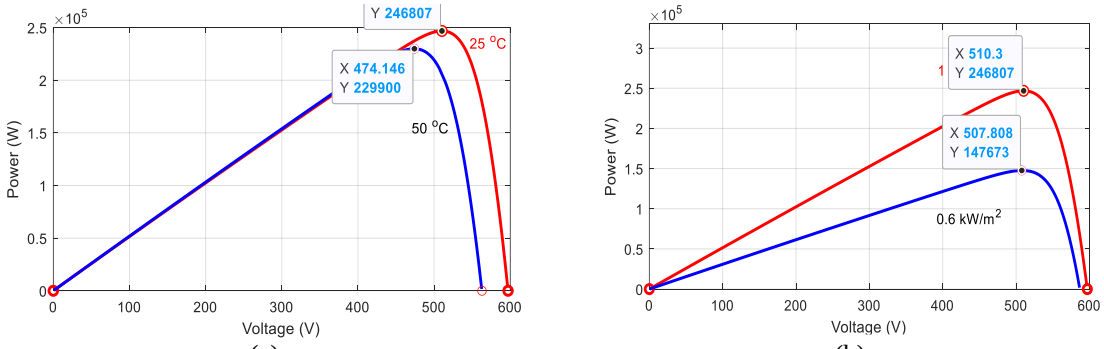

(a) (b)

Figure 8. P-V carves of PV panel of (a) Ir=1000 W/m^2 and (b) temp = 25 deg

3.2.1. INC MPPT controller

An MPPT system generally consists of a power converter integrated with an embedded control unit that executes a specific algorithm. Its primary function is to continuously maximize the extracted energy under varying Ir and temp conditions. Mathematically, the MPP of a PV module is attained when dP/dV = 0.

The incremental conductance (INC) algorithm capitalizes on this condition by comparing the incremental conductance, dI/dV, to the instantaneous conductance, −I/V. This comparison informs the controller of the operating point's position relative to the MPP, enabling appropriate voltage adjustments. Thanks to this mechanism, the INC method achieves stable tracking under dynamic environmental conditions. However, it may cause small oscillations around the MPP, which can compromise performance and efficiency. Figure 9 shows a flowchart of the INC algorithm.

3.2.2. FOPI MPPT controller

The FOPI regulator represents an advancement over the standard PI controller through fractional calculus, whose time-domain mathematical expression is written as (37) [34], [35].

$$U(t) = k_P\, e(t) + K_i D^{-\lambda} e(t) \quad (37)$$

Here, *u (t)* stands for the control signal, *e (t)* is the tracking error, with Kp and Ki designating the proportional and integral gains, respectively, and λ representing the fractional-order parameter. The frequency-domain representation of the FOPI controller is given by the following transfer function:

$$FOPI = \mathrm{k_P} + \frac{K_i}{S^{\lambda}} \tag{38}$$

The proposed PV system in this study employs an FOPI regulator to optimize the MPPT process. The controller receives only the tracking error as input, defined as the deviation of the power derivative with respect to voltage, dP/dV, from zero. Through dynamic adjustment of the control signal, the FOPI loop guides the PV array's operating point toward its optimum. Compared with conventional MPPT schemes, the proposed approach offers faster convergence to the MPP and substantially lower steady-state oscillations. As a result, the energy yield from the PV source is significantly enhanced. Figure 10 presents the complete block diagram of the proposed FOPI-based control architecture.

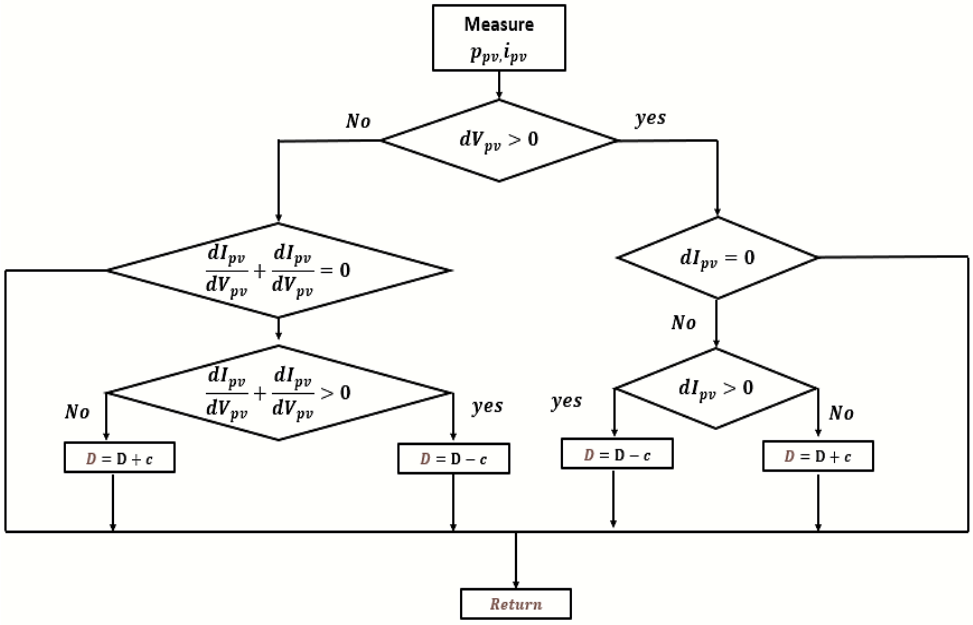

Figure 9. The flowchart of INC algorithm

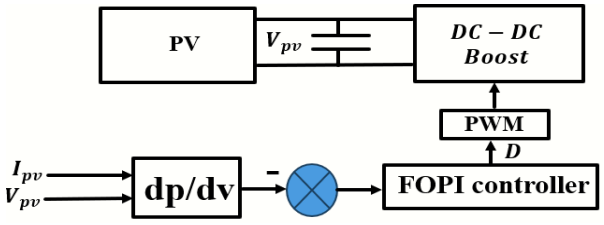

Figure 10. The block diagram of the improved control system of PVs using FOPI

4. RESULTS AND DISCUSSION

In order to assess the effectiveness of the control, strategies implemented and proposed herein under fluctuating environmental conditions, the irradiance and temperature profiles were varied according to the patterns depicted in Figures 11 and 12. The irradiance is increased from 600 W/m² to 1000 W/m² at t = 4 s, whereas the temperature is reduced from 50 °C to 25 °C at t = 0.2 s. The power extraction performance of the PV panels is illustrated in Figure 13. Among the control strategies compared, the conventional approach (S0) delivers the lowest output, reaching only 233.45 kW under nominal conditions, which translates into an efficiency of just 94.6%.

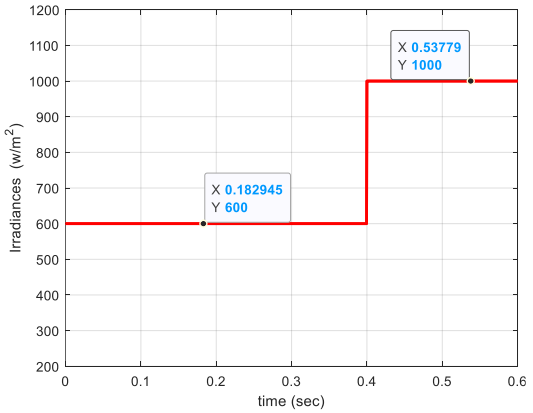

Figure 11. The irradiance profile

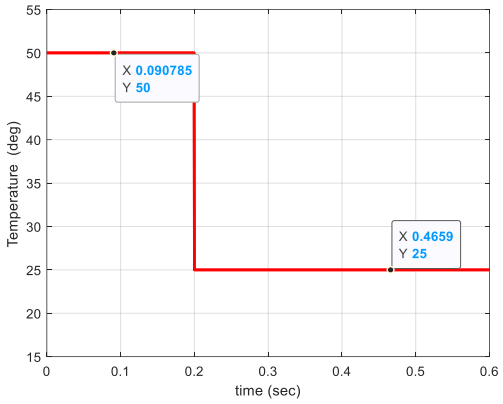

Figure 12. The temperature profile

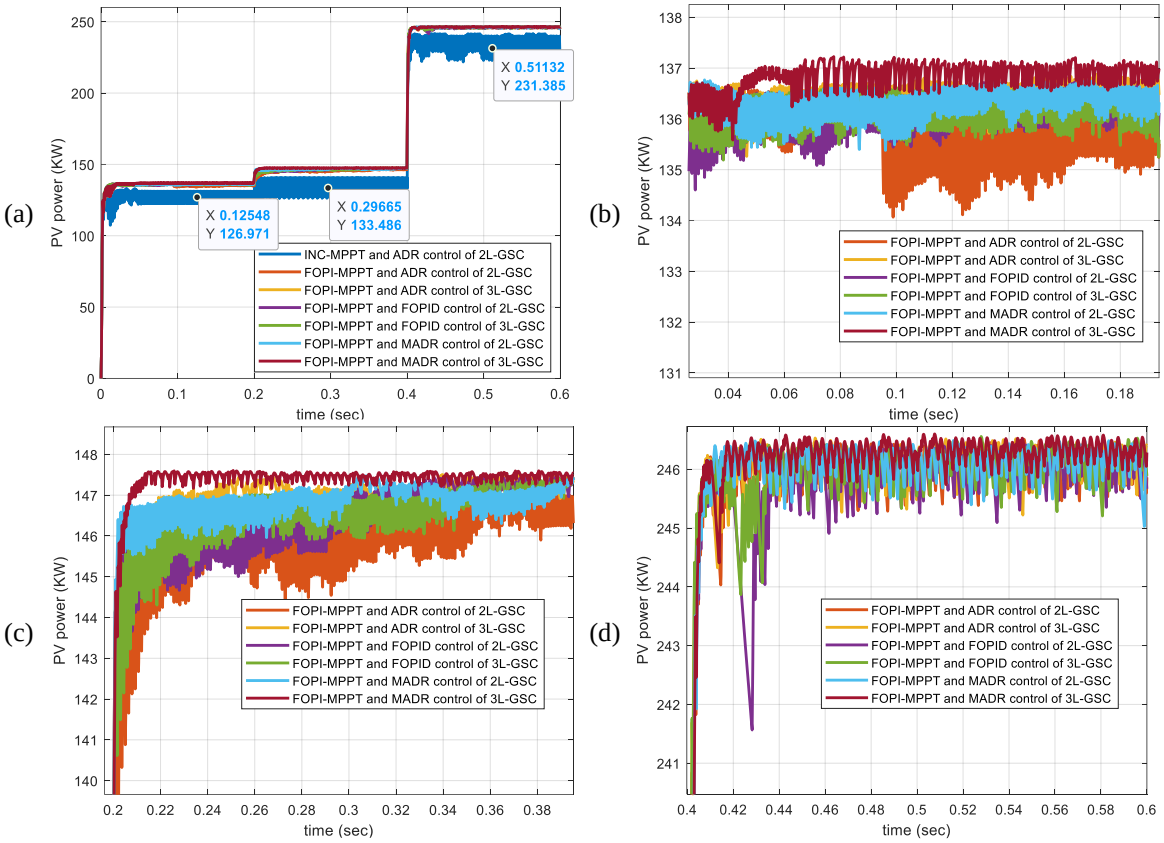

Figure 13. Response of PV power for: (a) time = 0-0.6 sec, (b) time = 0 sec-0.2 sec, (c) time = 0.2-0.4 sec, and (d) time = 0.4 sec-0.6 sec

With the use of the FOPI-based MPPT control system, a qualitative leap in efficiency is observed, ranging between 99.7% and 99.81%. For the use of the FOPI-ADRC system, the extracted power ranges between 246.1 kW when using a two-level inverter (S1) and 246.17 kW when using a three-level inverter (S2). However, with the use of the FOPI-FOPID system, the extracted power value reaches a value of 246.03 kW when using a two-level inverter (S3) and 246.14 kW when using a three-level inverter (S4). In contrast, the developed control strategy ensures accurate performance in tracking the MPP while effectively minimizing power fluctuations, as the extracted power at nominal environmental conditions reaches a value of 246.13 kW when using a two-level inverter (S5) and 246.33 kW when using a three-level inverter (S6), which means a high efficiency equal to 99.81%.

The enhanced performance exhibited by the proposed control strategy is attributable to a number of fundamental factors. First, compared to conventional or FOPI-ADRC systems, the system's ability to respond more quickly and flexibly to temperature and irradiance changes is made possible by the incorporation of the sophisticated control algorithms. Second, the technology ensures constant power output and increased overall efficiency by reducing oscillations around the maximum power point. Third, its dynamic response is improved, enabling quick voltage and current adjustments to preserve peak performance. Fourth, employing a multi-level inverter enhances power quality by lowering harmonics, which helps to extract energy more efficiently.

In order to confirm the performance of the proposed system, the DC-link voltage dynamics and the grid current THD profile are depicted in Figures 14 and 15, respectively. The results in Figure 14 show how well the proposed system works to achieve precise DC-link voltage regulation and maintain a stable and constant value that closely matches the reference. The system also shows less overshoot and deviation from the reference under temperature and irradiance variations. Additionally, the results in Figure 15 show how well the proposed system reduces THD, with an average value of 0.43%, as opposed to 2.87% when using the conventional control system. This aspect is of particular significance, as it improves power quality, minimizes energy losses within the grid and inverter, and facilitates more effective MPPT operation, thereby enhancing the overall system performance.

A comprehensive assessment of the control systems' performance requires an evaluation of the system's power transfer capability to the utility grid. Figures 16 and 17 present the active and reactive power delivered to the grid, respectively. The obtained results validate the effectiveness of the proposed control approach in preserving a unity power factor, while also attesting to its high-power transfer efficiency. Notably, the three-level inverter exhibits a slightly lower efficiency compared to the two-level topology, which can be attributed to the more sophisticated control requirements and elevated switching losses associated with multilevel configurations.

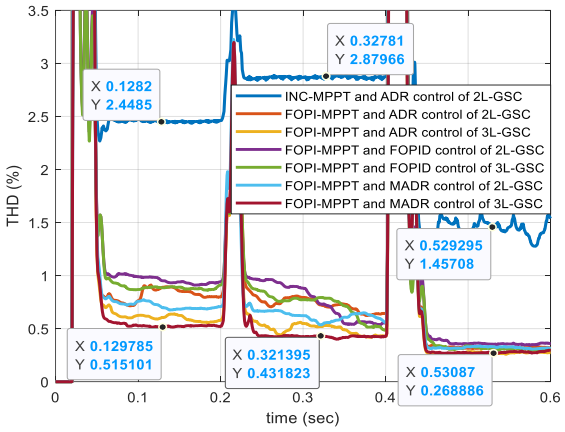

Figure 14. Response of DC-link voltage

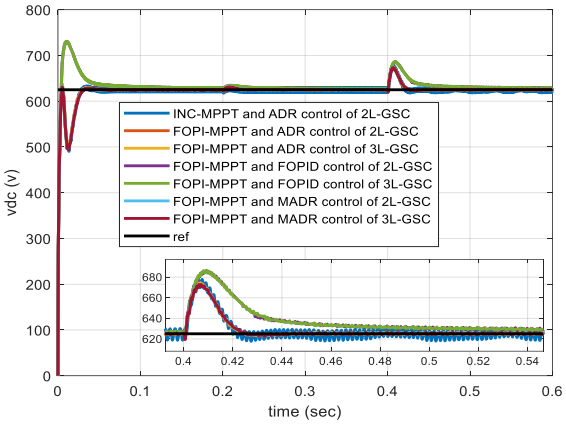

Figure 15. Response grid current THD

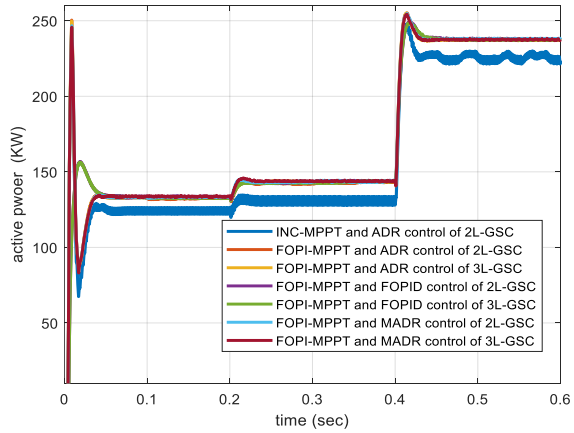

Figure 16. Response of grid active power

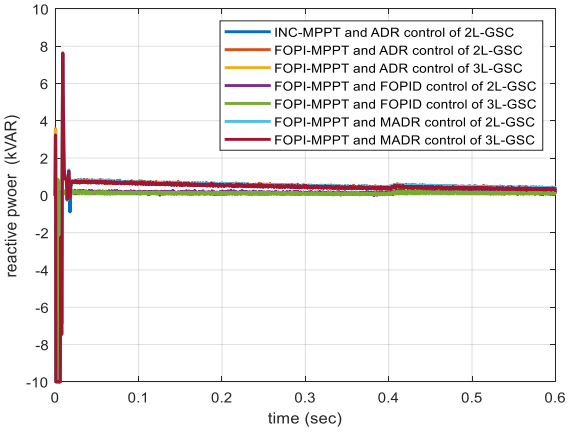

Figure 17. Response of grid reactive power

An overview of the performance of the control systems used and recommended in this study is given in Tables 1 and 2. It is evident that the conventional incremental conductance-active disturbance rejection control (INC–ADRC) system (S0) performs the worst, with a PV efficiency of 94.6% and an overall system efficiency of 91.27%. FOPI-based control systems, especially the proposed FOPI-MADRC system (S5 and S6), achieve the highest efficiencies while maintaining high extracted power, with up to 99.81% for PV and 96.33% for the system overall. The proposed FOPI-MADRC system shows the lowest THD of 0.43% (S6), indicating higher power quality, when compared to conventional and other sophisticated control methods. When taken as a whole, these results show how well the proposed system maximizes energy extraction, sustains stable operation, and improves power quality under minimal conditions.

Table 1. Control system comparison: efficiency and extracted power under 1000 W/m² and 25 °C

System	MPPT	VOC	Level	Extracted power (kW)	Eff of PV (%)	Grid power (kW)	Eff of all system (%)
S0	INC	ADRC	2	233.45	94.60	225.25	91.27
S1	FOPI	ADRC	2	246.10	99.72	237.69	96.31
S2	FOPI	ADRC	3	246.17	99.75	237.27	96.14
S3	FOPI	FOPID	2	246.03	99.67	237.7	96.31
S4	FOPI	FOPID	3	246.14	99.73	237.29	96.15
S5	FOPI	MADRC	2	246.13	99.73	237.74	96.33
S6	FOPI	MADRC	3	246.33	99.81	237.39	96.19

Table 2. Comparison of control systems used for the average THD of grid current

System	MPPT	VOC	Level	THD (%)
S0	INC	ADRC	2	2.87
S1	FOPI	ADRC	2	0.72
S2	FOPI	ADRC	3	0.49
S3	FOPI	FOPID	2	0.73
S4	FOPI	FOPID	3	0.71
S5	FOPI	MADRC	2	0.62
S6	FOPI	MADRC	3	0.43

5. CONCLUSION

This paper proposes and evaluates a two-stage control architecture for a three-level neutral-point-clamped (NPC) inverter within a grid-connected PV system, combining a fractional-order proportional-integral (FOPI) regulator with a modified active disturbance rejection controller (MADRC). The performance of the proposed approach was compared against the conventional INC–ADRC method and the FOPI–FOPID scheme, considering both two-level and three-level inverter topologies.

The obtained results confirm the enhanced energy harvesting capability of the proposed scheme, which delivers an extracted power of 246.33 kW, corresponding to a PV-side efficiency of 99.81% and a total system efficiency of 96.19%. These figures significantly outperform the 233.45 kW attained by the INC–ADRC architecture and compare favorably with the 246.14 kW yielded by the FOPI–FOPID strategy. Regarding current quality, the improvement is even more pronounced, with the total harmonic distortion (THD) dropping from 2.87% under INC–ADRC and 0.71% under FOPI–FOPID to only 0.43% when employing FOPI–MADRC.

It is worth noting a trade-off between efficiency and power quality: the two-level FOPI–MADRC setup exhibited a marginal edge in total system efficiency over its three-level counterpart, with values of 96.33% versus 96.19%, corresponding to a difference of just 0.14 percentage points. However, the three-level architecture successfully reduced the distortion factor substantially from 0.62% down to 0.43%, which positions the proposed scheme as the more attractive option for applications in which power quality constitutes the principal design criterion. Based on these observations, it is concluded that the three-level configuration based on FOPI–MADRC control constitutes a practical and efficient fundamental building block for future generations of grid-interfaced photovoltaic installations.

FUNDING INFORMATION

The authors state that no funding was involved in this research.

AUTHOR CONTRIBUTIONS STATEMENT

To recognize individual author contributions, reduce authorship-related conflicts, and promote collaboration, this journal adopts the Contributor Roles Taxonomy (CRediT) framework.

Name of Author	C	M	So	Va	Fo	I	R	D	O	E	Vi	Su	P	Fu
Gherici Dinar	✓	✓	✓	✓	✓	✓		✓	✓	✓	✓		✓	
Ahmed Tahour	✓	✓		✓	✓	✓	✓			✓		✓		

C : **C**onceptualization
M : **M**ethodology
So : **So**ftware
Va : **Va**lidation
Fo : **Fo**rmal analysis
I : **I**nvestigation
R : **R**esources
D : **D**ata Curation
O : Writing - **O**riginal Draft
E : Writing - Review & **E**diting
Vi : **Vi**sualization
Su : **Su**pervision
P : **P**roject administration
Fu : **Fu**nding acquisition

CONFLICT OF INTEREST STATEMENT

The authors confirm that there are no conflicts of interest associated with the research, authorship, or publication of this article.

DATA AVAILABILITY

The data that support the findings of this study are available in the article and the accompanying supplementary materials.

REFERENCES

[1] S. K. Kyei, H. K. Boateng, and A. J. Frimpong, "Renewable energy innovations: fulfilling SDG targets," *Clean Energy*, vol. 9, no. 2, pp. 190–203, Feb. 2025, doi: 10.1093/ce/zkae109.

[2] W. F. Pickard, "Smart grids versus the achilles' Heel of renewable energy: can the needed storage infrastructure be constructed before the fossil fuel runs out?," *Proceedings of the IEEE*, vol. 102, no. 7, pp. 1094–1105, Jul. 2014, doi: 10.1109/JPROC.2014.2316359.

[3] M. Ahmed, M. Abdelrahem, and R. Kennel, "Highly efficient and robust grid connected photovoltaic system based model predictive control with kalman filtering capability," *Sustainability*, vol. 12, no. 11, Jun. 2020, doi: 10.3390/su12114542.

[4] O. El Qouarti, T. Nasser, A. Essadki, I. Aboudrar, and M. Nadour, "Modeling, control study, and power management strategy of a hybrid grid-connected AC/DC microgrid with high integration of renewable energies and green hydrogen sources," *Clean Energy*, vol. 8, no. 6, pp. 296–324, Dec. 2024, doi: 10.1093/ce/zkae075.

[5] T. Zhu, J. Dong, X. Li, and S. Ding, "A comprehensive study on maximum power point tracking techniques based on fuzzy logic control for solar photovoltaic systems," *Frontiers in Energy Research*, vol. 9, Jul. 2021, doi: 10.3389/fenrg.2021.727949.

[6] M. J. K. Bashir, S. Abdelhak, W. A. Salah, and M. Abuhelwa, "Exploring public perception and willingness to pay for a renewable source of energy: evidence from an emerging economy of renewable-energy development," *Clean Energy*, vol. 8, no. 2, pp. 177–188, Apr. 2024, doi: 10.1093/ce/zkae016.

[7] H. J. El-Khozondar, R. J. El-Khozondar, K. Matter, and T. Suntio, "A review study of photovoltaic array maximum power tracking algorithms," *Renewables: Wind, Water, and Solar*, vol. 3, no. 1, Dec. 2016, doi: 10.1186/s40807-016-0022-8.

[8] P. Takun, S. Kaitwanidvilai and C. Jettanase, "Maximum power point tracking using fuzzy logic control for photovoltaic systems," *Proceedings of the International MultiConference of Engineers and Computer Scientists 2011*, vol. II, 2011.

[9] C. Boubii *et al.*, "Integrated control and optimization for grid-connected photovoltaic systems: a model-predictive and PSO approach," *Energies*, vol. 16, no. 21, p. 7390, Nov. 2023, doi: 10.3390/en16217390.

[10] M. Tivanov, A. Moskalev, I. Kaputskaya, and P. Żukowski, "Obliczanie maksymalnej sprawności złącza p-n ogniw słonecznych na podstawie współczynnika absorpcji półprzewodników)," *Przeglad Elektrotechniczny*, vol. 92, no. 8, pp. 85–87, 2016, doi: 10.15199/48.2016.08.23.

[11] Y. H. Sim, M. J. Yun, S. I. Cha, S. H. Seo, and D. Y. Lee, "Improvement in energy conversion efficiency by modification of photon distribution within the photoanode of dye-sensitized solar cells," *ACS Omega*, vol. 3, no. 1, pp. 698–705, Jan. 2018, doi: 10.1021/acsomega.7b01618.

[12] F. Sebaaly, H. Vahedi, H. Y. Kanaan, N. Moubayed, and K. Al-Haddad, "Design and implementation of space vector modulation-based sliding mode control for grid-connected 3L-NPC inverter," *IEEE Transactions on Industrial Electronics*, vol. 63, no. 12, pp. 7854–7863, Dec. 2016, doi: 10.1109/TIE.2016.2563381.

[13] Y. Yang and F. Blaabjerg, "Overview of single-phase grid-connected photovoltaic systems," *Electric Power Components and Systems*, vol. 43, no. 12, pp. 1352–1363, Jul. 2015, doi: 10.1080/15325008.2015.1031296.

[14] B. Afif, M. Salmi, M. Berka, and U. Özkaya, "Enhancing efficiency and power quality in grid-connected photovoltaic systems based on linear matrix inequality methodology," *Electrical Engineering*, vol. 107, no. 10, pp. 12739–12752, Oct. 2025, doi: 10.1007/s00202-025-03173-w.

[15] G. Tsengenes and G. Adamidis, "A multi-function grid connected PV system with three level NPC inverter and voltage oriented control," *Solar Energy*, vol. 85, no. 11, pp. 2595–2610, Nov. 2011, doi: 10.1016/j.solener.2011.07.017.

[16] G. Dinar and A. Tahour, "Control of multi-level NPC inverters in PV/grid systems using ADRC and MADRC," *Indonesian Journal of Electrical Engineering and Computer Science*, vol. 41, no. 2, Feb. 2026, doi: 10.11591/ijeecs.v41.i2.pp456-469.

[17] H. Can, "Model of a photovoltaic panel emulator in MATLAB-Simulink," *Turkish Journal of Electrical Engineering and Computer Sciences*, Jan. 2013, doi: 10.3906/elk-1105-29.

[18] J. I. Rosell and M. Ibáñez, "Modelling power output in photovoltaic modules for outdoor operating conditions," *Energy Conversion and Management*, vol. 47, no. 15–16, pp. 2424–2430, Sep. 2006, doi: 10.1016/j.enconman.2005.11.004.

[19] A. A. Hocine, T. Mustapha, D. E. Chaouch, and K. Brahim, "An offline trained artificial neural network to predict a photovoltaic panel maximum power point," *Revue Roumaine des Sciences Techniques Serie Electrotechnique et Energetique*, vol. 61, no. 3, pp. 255–257, 2016.

[20] F. A. Mohammed, M. E. Bahgat, S. S. Elmasry, and S. M. Sharaf, "Design of a maximum power point tracking-based PID controller for DC converter of stand-alone PV system," *Journal of Electrical Systems and Information Technology*, vol. 9, no. 1, Dec. 2022, doi: 10.1186/s43067-022-00050-5.
[21] N. Li, S. Zhang, Z. Xiao, Z. An, Y. Zhang, and L. Jiang, "Bypass inductor type LCL filter parameter optimization for three-level grid-connected converter," *Frontiers in Energy Research*, vol. 10, Mar. 2022, doi: 10.3389/fenrg.2022.852046.
[22] R. Errouissi, A. Al-Durra, and S. M. Muyeen, "Offset-free feedback linearisation control of a three-phase grid-connected photovoltaic system," *IET Power Electronics*, vol. 9, no. 9, pp. 1933–1942, Jul. 2016, doi: 10.1049/iet-pel.2015.0961.
[23] I. Aboudrar, S. El Hani, H. Mediouni, A. Aghmad, and M. S. Heyine, "Robust control of three phase grid connected PV system based on ADRC and fuzzy," in *2018 6th International Renewable and Sustainable Energy Conference (IRSEC)*, IEEE, Dec. 2018, pp. 1–6, doi: 10.1109/IRSEC.2018.8702950.
[24] I. M.-B. Hassine, M. W. Naouar, and N. Mrabet-Bellaaj, "Model based predictive control for three-phase grid connected converter," *Journal Electrical Systems*, vol. 11, no. 4, pp. 463–475, 2015.
[25] M. A. George, D. V. Kamat, and T. Indiran, "OTA-C realization of an optimized FOPID controller for BLDC motor speed control," *IETE Journal of Research*, vol. 69, no. 1, pp. 118–136, Jan. 2023, doi: 10.1080/03772063.2021.1951380.
[26] W. Zheng, Y. Chen, X. Wang, M. Lin, and J. Guo, "Robust fractional order PID controller synthesis for the first order plus integral system," *Measurement and Control*, vol. 56, no. 1–2, pp. 202–214, Jan. 2023, doi: 10.1177/00202940221095564.
[27] I. Pan and S. Das, "Frequency domain design of fractional order PID controller for AVR system using chaotic multi-objective optimization," *International Journal of Electrical Power & Energy Systems*, vol. 51, pp. 106–118, Oct. 2013, doi: 10.1016/j.ijepes.2013.02.021.
[28] S. Tufenkci, B. B. Alagoz, B. Senol, and R. Matušů, "An overview of FOPID controller design in v-domain: design methodologies and robust controller performance," *International Journal of Systems Science*, vol. 54, no. 11, pp. 2316–2336, Aug. 2023, doi: 10.1080/00207721.2023.2230200.
[29] Z. Chen, Y. Wang, M. Sun, and Q. Sun, "Convergence and stability analysis of active disturbance rejection control for first-order nonlinear dynamic systems," *Transactions of the Institute of Measurement and Control*, vol. 41, no. 7, pp. 2064–2076, Apr. 2019, doi: 10.1177/0142331218794812.
[30] Z. Duan, C. Sun, J. Li, and Y. Tan, "Research on servo valve-controlled hydraulic motor system based on active disturbance rejection control," *Measurement and Control*, vol. 57, no. 2, pp. 113–123, Feb. 2024, doi: 10.1177/00202940231194115.
[31] A. Boukhriss, "Active disturbance rejection control applied to a three-phase grid-connected photovoltaic system," *Advances in Electrical and Computer Engineering*, vol. 22, no. 1, pp. 87–94, 2022, doi: 10.4316/AECE.2022.01010.
[32] H. Laghridat, A. Essadki, and T. Nasser, "Comparative analysis between PI and linear-ADRC control of a grid connected variable speed wind energy conversion system based on a squirrel cage induction generator," *Mathematical Problems in Engineering*, vol. 2019, no. 1, Jan. 2019, doi: 10.1155/2019/8527183.
[33] Y. Xia, B. Liu, and M. Fu, "Active disturbance rejection control for power plant with a single loop," *Asian Journal of Control*, vol. 14, no. 1, pp. 239–250, Jan. 2012, doi: 10.1002/asjc.240.
[34] D. Xue, *Fractional-order control systems*. De Gruyter, 2017, doi: 10.1515/9783110497977.
[35] H. Meneses, O. Arrieta, F. Padula, A. Visioli, and R. Vilanova, "FOPI/FOPID tuning rule based on a fractional order model for the process," *Fractal and Fractional*, vol. 6, no. 9, Aug. 2022, doi: 10.3390/fractalfract6090478.

BIOGRAPHIES OF AUTHORS

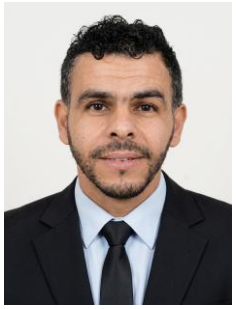

Gherici Dinar was born in 1987 and is a Ph.D. student at Mustapha Stambouli University of Mascara, Algeria. He previously worked at the Portuguese company EURL EFACEC in the electrical network sector and is currently employed by SONELGAZ, an electricity distribution company. His research interests include energy management, power grid optimization, nonlinear control, and renewable energy in electrical engineering. He can be contacted at email: dnr.ghrc@gmail.com.



Ahmed Tahour was born in 1972 in Ouled Mimoun, Tlemcen, Algeria. He received his bachelor's degree in electrical engineering in 1996, his master's degree in 1999, and his Ph.D. degree in 2007, all from the Institute of Electrical Engineering, University of Sidi Bel Abbès, Algeria. He is currently a professor of electrical engineering at the Higher School of Applied Sciences of Tlemcen, Algeria. He serves as an editor for the International Journal of Electrical and Electronics Engineering (IJEAEEE) and as a reviewer for RRST and Elsevier journals, including the International Journal of Electrical Power & Energy Systems (IJEPES) and Computers & Electrical Engineering (CEP). He has also served as a reviewer and member of the international program committees for the SEB (2014–2023) and ICRERA (2014–2025) conferences. His research interests include power electronics, electrical machine control, and renewable energy. He can be contacted at email: tahourahmed@yahoo.fr.